




Photon recycling in nanopatterned perovskite thin-films for photovoltaic applications

Cite as: APL Photonics 4, 076104 (2019); <https://doi.org/10.1063/1.5094579>

Submitted: 04 March 2019 . Accepted: 01 July 2019 . Published Online: 24 July 2019

Stefan Nanz, Raphael Schmager, Muluneh G. Abebe, Christian Willig, Andreas Wickberg , Aimi Abass, Guillaume Gomard , Martin Wegener, Ulrich W. Paetzold , and Carsten Rockstuhl



View Online



Export Citation



CrossMark

ARTICLES YOU MAY BE INTERESTED IN

[Absolute photoluminescence intensity in thin film solar cells](#)

Journal of Applied Physics **125**, 053103 (2019); <https://doi.org/10.1063/1.5064798>

[Large-area enhancement of far-field fluorescence intensity using planar nanostructures](#)

APL Photonics **4**, 076101 (2019); <https://doi.org/10.1063/1.5096270>

[Pushing the limits of deep-ultraviolet scanning near-field optical microscopy](#)

APL Photonics **4**, 070801 (2019); <https://doi.org/10.1063/1.5097865>

additive manufacturing epitaxial crystal growth cerium oxide polishing powder silver nanoparticles sputtering targets III-IV semiconductors CVD precursors europium phosphors

AMERICAN ELEMENTS
THE ADVANCED MATERIALS MANUFACTURER®

deposition slugs OLED Lighting spintronics solar energy osmium nanoribbons thin films chalcogenides AuNPs GDC Li-ion battery electrolytes 99.999% ruthenium spheres

endohedral fullerenes copper nanoparticles diamond micropowder CIGS MBE grade materials palladium catalysts flexible electronics beta-barium borate borosilicate glass dysprosium pellets YBCO pyrolytic graphite 3d graphene foam indium tin oxide mesoporous silica raman substrates sapphire windows tungsten carbide InGaAs barium fluoride carbon nanotubes lithium niobate scandium powder

gallium lump glassy carbon nanodispersions InAs wafers laser crystals ultra high purity materials MOFs surface functionalized nanoparticles organometallics quantum dot Al Si P S Cl Ar rare earth metals photovoltaics refractory metals MOCVD superconductors transparent ceramics ultra high purity silicon

American Elements opens up a world of possibilities so you can **Now Invent!**

Over 15,000 certified high purity laboratory chemicals, metals, & advanced materials and a state-of-the-art Research Center. Printable GHS-compliant Safety Data Sheets. Thousands of new products. And much more. All on a secure multi-language "Mobile Responsive" platform.

perovskite crystals yttrium iron garnet alternative energy h-BN gold nanocubes graphene oxide macromolecules photonics rhodium sponge fiber optics beamsplitters infrared dyes zeolites fused quartz metallocenes platinum ink buckyballs Ti-6Al-4V

Now Invent.™
The Next Generation of Material Science Catalogs

www.americanelements.com

Photon recycling in nanopatterned perovskite thin-films for photovoltaic applications

Cite as: APL Photon. 4, 076104 (2019); doi: 10.1063/1.5094579

Submitted: 4 March 2019 • Accepted: 1 July 2019 •

Published Online: 24 July 2019



View Online



Export Citation



CrossMark

Stefan Nanz,^{1,a)} Raphael Schmager,² Muluneh G. Abebe,¹ Christian Willig,² Andreas Wickberg,³  Aimi Abass,⁴ Guillaume Gomard,^{2,5}  Martin Wegener,³ Ulrich W. Paetzold,^{2,5}  and Carsten Rockstuhl^{1,4}

AFFILIATIONS

¹Institute of Theoretical Solid State Physics, Karlsruhe Institute of Technology, 76131 Karlsruhe, Germany

²Institute of Microstructure Technology, Karlsruhe Institute of Technology, 76344 Eggenstein-Leopoldshafen, Germany

³Institute of Applied Physics, Karlsruhe Institute of Technology, 76131 Karlsruhe, Germany

⁴Institute of Nanotechnology, Karlsruhe Institute of Technology, 76021 Karlsruhe, Germany

⁵Light Technology Institute, Karlsruhe Institute of Technology, 76131 Karlsruhe, Germany

^{a)}Electronic mail: stefan.nanz@kit.edu

ABSTRACT

Perovskites are a class of recently established materials that triggered enormous interest particularly for solar cell applications. Recent studies have pointed out the extraordinary luminescence quantum yield in perovskite materials. The concept of photon recycling investigated in this work promises a route to reharvest the radiatively emitted photons and, thus, lead to an increase in the open-circuit voltage in perovskite solar cells. In this light, this work investigates the role of nanostructured perovskite absorber layers. While the change of the open-circuit voltage due to photon recycling is understood at a conceptual level, the actual impact of a nanostructured interface on the photon recycling has not yet been studied quantitatively. Here, we rely on full-wave optical simulations to quantify the impact of photon recycling on the open-circuit voltage in a nanotextured biperiodic perovskite thin-film layer and additionally with the perovskite layer integrated into a complete solar cell multilayer stack. The validity of the optical simulations is confirmed by far-field measurements of the emission characteristics from fabricated devices. We find that the considered nanostructure provides around 2% increase to a typically achievable open-circuit voltage in perovskite solar cells. We thereby show that, while the main focus for the design of nanostructures is the optimization of light harvesting, photon recycling might be of interest in future designs of solar cell devices.

© 2019 Author(s). All article content, except where otherwise noted, is licensed under a Creative Commons Attribution (CC BY) license (<http://creativecommons.org/licenses/by/4.0/>). <https://doi.org/10.1063/1.5094579>

I. INTRODUCTION AND MOTIVATION

Hybrid organic-inorganic metal halide perovskites (called here perovskites) are an outstandingly promising novel material class for thin-film photovoltaics (PV) and light emission devices.^{1–3} The deposition of such perovskite materials is possible with inexpensive fabrication processes and with low-cost precursor materials.⁴ Furthermore, the bandgap of these perovskites can be tuned by compositional engineering of the crystal structure. This makes them suitable for tandem photovoltaics and allows for lighting applications such as lasers and LEDs for a wide range of wavelengths.^{5–8}

Given the fundamental reciprocity relation, light absorbed in the perovskite semiconductor thin-film of a solar cell or LED can also be emitted radiatively. For high quality perovskite thin-films,

this luminescence is very prominent⁹ since the competing parasitic absorption and nonradiative recombination processes are heavily reduced. This is astonishing since perovskite thin-films are of multicrystalline morphology and exhibit a large amount of grain boundaries, in contrast to other highly luminescent semiconductors such as epitaxially grown GaAs thin-films. As a consequence of the dominant radiative recombination,¹⁰ perovskite thin-films feature photon recycling, which describes the process of reabsorption of previously radiatively emitted light in the absorber.^{11–14} Since the open-circuit voltage (V_{oc}) denotes the point of equilibrium of photons absorbed by the perovskite absorber layer of a solar cell and the photons recombined (radiatively and nonradiatively) and parasitically absorbed, photon recycling bears the promise to enhance the V_{oc} .

Although photon recycling has not yet been observed in prototype perovskite solar cells, which suffer next to the nonradiative recombination also from parasitic absorption, the effect is of high conceptual relevance and should already be significant if currently achievable nonradiative lifetimes are assumed.^{15,16} For planar and randomly textured multilayer structures, the impact of photon recycling has already been quantified using ray-optical methods and a statistical treatment of the absorption due to the random interface, respectively.^{15,17–19} Rigorous analyses have been done so far only for planar multilayers.^{20,21}

The predominant improvement in efficiency is obtained by maximizing the short-circuit current density, which directly depends on the absorbed portion of the incoming light. Therefore, thin-film nanostructures with periodic nanotextures have been extensively analyzed and prototyped for improved current generation in perovskite solar cells.^{22–24} On the one hand, photon recycling will be reduced compared to planar layers when using light trapping structures due to more available outcoupling channels so that the portion of reabsorbed photons is decreased.^{15,20} The increased light-incoupling into the cell, however, will be more beneficial in the presence of nanotextured interfaces, implying a trade-off between increasing the short-circuit current density and the open-circuit voltage. Therefore, it is of key importance to understand how the light emission and open-circuit voltage are impacted by photon recycling in nanostructured perovskite thin-films.

The calculation of the enhancement of the open-circuit voltage due to photon recycling, ΔV_{oc}^{PR} , is demanding for nanotextured interfaces, both numerically and experimentally. In numerics, wave-optical effects have to be considered and emission characteristics of single emitters placed in periodic or quasiperiodic environments have to be calculated. Experimentally, the portion of the reemitted power that is parasitically absorbed or escapes the device radiatively has to be measured, which is a very difficult task. However,

the additional gain in open-circuit voltage is not negligible and a careful analysis is desirable for a full understanding of the effect of nanostructuring solar cell interfaces. Therefore, the presence of a light-trapping nanostructure prompts for an in-depth rigorous wave-optical analysis regarding the importance of photon recycling, and we investigate it in this work.

In the following, we will investigate the photon-recycling capabilities of a periodically nanostructured thin-film perovskite layer. First, a simplified multilayer is considered because the luminescence measurements were experimentally easier realizable without a back reflector. The emission characteristics and the far field angular spectrum of this simplified layer stack are measured and numerically calculated. We will show that the relevant angular spectrum features are intimately linked to the supported guided modes. From the numerical simulations, we obtain the portion of emitted power that is absorbed in the different layers or escapes radiatively out of the structure. Using these quantities, we can calculate ΔV_{oc}^{PR} . Afterwards, we numerically study a complete solar cell stack and again calculate ΔV_{oc}^{PR} .

We first consider the multilayer layout shown in Fig. 1(a). The key part of our stack is a perovskite layer; its total thickness varies in the simulations between 160 nm and 250 nm, which are at the lower end of the typical thickness range of thin-film perovskite solar cells. Below the perovskite, a 148 nm thick indium tin oxide (ITO) layer atop a (semi-infinite) glass substrate is assumed. With the latter, we mimic the several millimeter thick glass substrate that is present in the measurements. Above the perovskite thin-film, we assume air. This stack enables feasible measurements of the luminescence and hence provides a useful reference system for our numerical calculations. At the perovskite/air interface, a square grating of cylindrical holes is assumed. Its pitch size is set to 400 nm, corresponding to the optimized value for light-trapping.²⁴ The hole depth was chosen to be 110 nm, and the hole diameter was chosen to be 285 nm. This resembles a typical light in-coupling/light-trapping

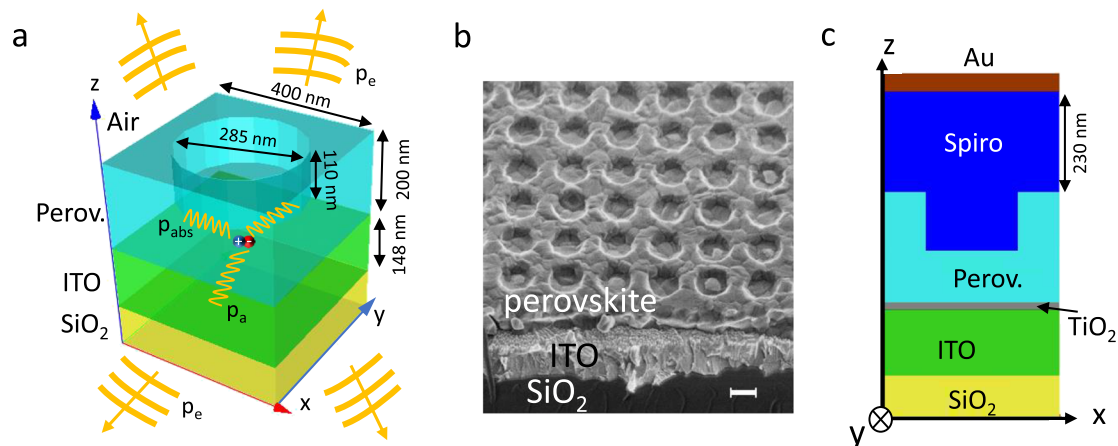


FIG. 1. (a) Three-dimensional view of the considered nanostructured multilayer consisting of a glass substrate, ITO, and perovskite (in this example with a thickness of 200 nm). The perovskite/air interface is imprinted with a cylindrical grating. p_a is the parasitically absorbed power in the ITO, whereas p_e is the portion of the power that radiatively escapes the device. (b) Scanning-electron microscope image of the imprinted multilayer taken under an angle of 45°. The scale bar indicates 200 nm. (c) Complete solar cell stack featuring a hole-transport layer (Spiro-OMeTAD, thickness 230 nm, denoted in the illustration as “Spiro”), an electron-transport layer (TiO₂, thickness 20 nm), and a gold back reflector.

nanotexture, and similar geometries have also been shown to enhance the photoluminescence (PL) of perovskite cells.²⁵ For reference, two additional perovskite/air interfaces have also been investigated: a planar interface and a Lambertian scattering interface.

The analysis we present consists of three steps. Initially, we will study the emission characteristics of spatially distributed dipole emitters in the perovskite thin-film while considering the presence of one of the three types of interfaces. This allows us to distinguish the fraction of the absorbed light and of the light that is radiated out of the device. To confirm these numerical simulations, we will then compare simulated emission patterns with those that are measured from fabricated devices. We demonstrate qualitative agreement between our simulated results and the measurements. Based on the simulated reabsorption, we will predict the enhancement of the open-circuit voltage due to photon recycling, ΔV_{oc}^{PR} . This last step is done for both the simplified stack and also the complete solar cell stack displayed in Fig. 1(c). Even though studied here for specific grating profiles, our approach is sufficiently versatile and constitutes an important tool in the ongoing research to capitalize on and improve the photon recycling in perovskite thin-film solar cells.

II. METHODS

A. Fabrication of samples

Indium tin oxide (ITO) substrates from Luminescence Technology were cleaned in ultrasonic baths of acetone and isopropanol for 15 min each. After additional oxygen plasma cleaning, the methylammonium lead triiodide perovskite (MAPbI₃) solution was spin-coated in nitrogen atmosphere at 3000 rpm for 30 s. Further experimental details of the fabrication are described in a previous publication.²⁶ To anneal the absorber layer, the sample was heated for 10 min at 115 °C. The refractive index and extinction coefficient of the so obtained perovskite were already measured and published in the past.²⁷

The perovskite surface was afterwards imprinted via thermal nanoimprint lithography with a mold to achieve a grating texture at the air side.²⁸ The imprint was performed at 100 °C for 10 min with a pressure of 300 bars. As a mold, a glass substrate with a textured UV curable resist (OrmoStamp, Micro Resist Technology) is used. In Fig. 1(b), a scanning-electron microscope (SEM) image of one of the fabricated samples is shown. The period of the two-dimensional grating is ~400 nm, and the perovskite thickness is ~250 nm. As was shown in several publications, such thermal imprint does not impair the crystal structure. Therefore, also the photoluminescence properties of perovskite are not negatively affected, and they might even be improved.^{28–30}

B. Experimental setup

The angle-resolved emission measurements of the imprinted perovskite layers are obtained with an in-house microscopy system using a 63× objective lens with a numerical aperture of 0.75 (LD Plan Neofluar). A scheme of the setup is shown in Fig. S1. The perovskite sample is excited with a pulsed and focused Ti:Sa laser at 690 nm from the nanostructured side. The emission is collected by the

objective lens on the side of the glass substrate in transmission. Subsequently, the laser beam is filtered out with a 700 nm long pass filter and the back focal plane of the objective lens is imaged onto a CCD camera (Princeton Instruments LN-CCD-1340/100-EB/1) with the exposure time set to 1 s. Using this approach, the PL emission can be viewed in reciprocal space.

C. Numerical analysis

From supporting measurements of the spectrally resolved emission from the perovskite layers, we find that the emission peak of the used perovskite thin-film is at 780 nm (see also Fig. S2). We use this wavelength in all further calculations, hereby assuming that the emission at shorter and longer wavelengths has a compensatory effect and does not significantly affect the photon recycling. The optical indices used in the simulations are $n_{ITO} = 1.62 + 0.02i$, $n_{Perov} = 2.58 + 0.04i$, $n_{SiO_2} = 1.45$. Besides, the virtual nonabsorbing layer is modeled with $n_{art} = \Re\{n_{Perov}\} = 2.58$.

1. Optical simulations of the planar interfaces

To study the reabsorption in the presence of planar interfaces, our calculations have been performed using the FEM solver JCMsuite.³¹ The considered layer stack consisted of a semi-infinite glass half-space, an ITO layer (148 nm), the perovskite layer (different thicknesses), and a semi-infinite air half-space. For the simulations, we considered a three-dimensional unit cell with perfectly matched layers (PMLs) at all boundaries to avoid unphysical reflections.³² In the x - and y -directions, a sufficient large spatial extent was chosen, i.e., 400 nm. We simulated a dipole emitter enclosed in a small cylindrical cavity of a nonabsorbing perovskite with height and diameter of 40 nm. Such an enclosure had to be considered because the calculation of an emission response in an absorbing medium cannot be done without assuming a lower cutoff distance of the dipole emitter to the absorber medium.^{33,34}

The dipole emitter was placed at three different vertical positions inside the perovskite: in the center, 25 nm away from the perovskite/air interface, and also 25 nm away from the perovskite/ITO interface. Hereby, we obtain a sufficient spatial resolution of the varying local density of states due to the excited modes in the multilayer system. At each position, we simulated for the three discrete orientations in x -, y -, and z -directions. We calculated the absorptance in the perovskite thin-film for each position and orientation by integration of the divergence of the Poynting vector in the perovskite domain and adding the power flux that left the perovskite through the side boundaries in x - and y -directions. We then averaged the absorptance for the three positions and orientations.

2. Optical calculations with the Lambertian interface

To study the reabsorption in the presence of a Lambertian interface, we analyzed the situation analytically using expressions documented in prior literature given by Green.³⁵ These expressions are exact if the extinction coefficient is small compared to the real part of the refractive index, a condition which applies in good approximation to the considered situation. This analytical framework allows us to calculate the total absorptance in the perovskite layer stack. More details are documented for completeness in the [supplementary material](#). We consider separately the three possible

orientations x , y , and z for the electric dipole emitter and different vertical positions inside the perovskite layer and take the average absorbance across all configurations.

3. Optical simulations of the grating structures

To study the reabsorption in the presence of the grating structure, we considered the emission of a dipole placed in the structured perovskite layer (see Fig. 1). In the simulations, the horizontal boundaries were set to be periodic, and the top and bottom boundaries were chosen to be PMLs to suppress nonphysical reflections. The perovskite/air interface was textured with cylindrical holes with a diameter of 285 nm and a depth of 110 nm.

The rigorous calculation of a single dipole placed in a periodic environment is computationally not feasible: One might use a very large computational domain, but the amount of unit cells that would be required to be sure that the dipole radiation has been fully absorbed or radiated would be beyond reasonable computational resources. In the case of periodic boundary conditions, the dipole would also be repeated periodically. This would cause coherent effects of the dipole emission and would thus yield wrong results for our system. Because of these problems, we make use of the inverse Floquet transformation.³⁶ This provides a way to simulate a large number of periodic dipoles with the unit cell as the computational domain, but each dipole has a different phase. With a superposition of the resulting fields in Fourier space, one can reconstruct the effective radiation response of an isolated dipole. We discretize the Bloch vector along both x - and y -axes in 64 values, which provides enough accuracy while still being computationally feasible. The angular spectrum was then reconstructed by superposing the simulation results for different phases.

To properly resolve the spatial dependence of the emission inside the perovskite layer, we distribute the emitters in the perovskite for the simulations. At each z -position, emitters at four different positions are calculated: edge, corner, half-diagonal, and center (only in the bulk region) and just outside the hole (only in the grating region). Along the z -direction, the simulated dipole positions are laterally spaced in steps of 10 nm, and each emitter response is calculated for x -, y -, and z -polarization. Simulating the emitters in only one of the four quadrants of the unit cell leads to an asymmetric angular spectrum. Therefore, we rotated the results of the simulated horizontal positions according to the underlying symmetry of the structure to retrieve a correspondingly rotational symmetric angular spectrum. The average angular spectrum, which will be compared to measurements, is then obtained from averaging over the three polarizations and various vertical and horizontal positions.

For the simplified layer stack, we calculated both the angular spectrum of the far field in the positive and negative z -directions, respectively. In the negative z -direction, the fields inside the semi-infinite glass half-space were projected onto purely s - and p -polarized fields, respectively, and then the Fresnel coefficients were used to calculate the transmitted fields into air. Both angular spectra, in the positive and negative z -directions, are qualitatively similar and differ mainly in the total power and the presence of some minor additional features in the far field at the glass side, so we will only show the angular spectra of the negative z -direction since the measurements were also done in this half-space.

Besides the inverse Floquet method, we have to slightly modify our simulation unit cell and enclose, like in the case for the planar geometry, our emitter in a small cavity of nonabsorbing perovskite. Instead of a cylindrical enclosure like in the planar case, we use a slab with diameter 40 nm that spans the whole unit cell. We also ensure that both in the bulk and in the grating region, there is always a thin absorbing perovskite between any adjacent material and the nonabsorbing enclosure. The reason for using a slab is to speed up computation time since several dipole emitters at the same vertical position can be simulated with the same geometry. This greatly reduces the calculation time due to reduction of necessary matrix inversions in the process of the FEM solving.

4. Estimation of the open-circuit voltage enhancement

Based on the comprehensive thermodynamical treatment of photon management in solar cells by Rau *et al.*,³⁷ it was shown by Kirchartz *et al.*¹⁵ for planar and Lambertian textures that photon recycling can provide a significant contribution to the total open-circuit voltage. The analysis was extended by Abebe *et al.*²⁰ to account for situations where rigorous wave-optical calculations are required to determine ΔV_{oc}^{PR} . Their treatment yielded a formula to calculate the open-circuit voltage enhancement due to photon recycling, ΔV_{oc}^{PR} , for arbitrary structures, as long as the absorption in all layers and the probability of radiative emission can be determined using rigorous methods,

$$\Delta V_{oc}^{PR} = \frac{k_B T_c}{e} \ln \left(\frac{1}{1 - (1 - p_e - p_a) Q_{lum}} \right). \quad (1)$$

p_a and p_e are the probabilities that a regenerated photon is parasitically absorbed and is radiatively emitted, respectively. k_B is the Boltzmann constant, e is the elementary charge, and T_c is the temperature at which the solar cell is operated, which we assume here to be $T_c = 300$ K.

Furthermore, we assume that only radiative recombination processes occur, i.e., we set the internal quantum luminescence efficiency $Q_{lum} = 1$. With this assumption, the calculated results provide an upper boundary for ΔV_{oc}^{PR} that is actually achievable in an experimental setup. The probabilities of parasitic absorption and radiative emission are impossible to determine in experiment, and we therefore calculate them from our simulations. Since $1 - p_e - p_a = p_{abs}$, we can also just use the portion of power that is absorbed in the perovskite layer resulting from the dipole emission.

5. Calculation of the short-circuit current density

To calculate the short-circuit current density, we perform FEM calculations with linear polarized plane waves that are incident onto the multilayer stack from the negative z -direction, i.e., from the ITO-coated side. We use periodic boundary conditions in the x - y -plane and PMLs along the z -direction. We consider the wavelength range 330 nm–820 nm and simulate in steps of 5 nm. The refractive index data in this wavelength range were measured by us before.³⁷ The absorbance $A(\lambda)$ in the perovskite layer is obtained with JCMsuite through an integration of the Poynting vector in the perovskite

volume. We then calculate the short-circuit current density j_{sc} with the formula³⁸

$$j_{sc} = e \int_{330 \text{ nm}}^{820 \text{ nm}} A(\lambda) \cdot \phi(\lambda) \cdot IQE \, d\lambda. \quad (2)$$

$\phi(\lambda)$ is the AM 1.5G solar irradiation photon number spectrum³⁹ and e is the elementary charge. We assume perfect collection of the generated electron-hole pairs; thus, the internal quantum efficiency is chosen to be $IQE = 1$.

III. RESULTS

The reabsorption in the perovskite layer for the planar and Lambertian interfaces is first studied according to the calculations described in Secs. II C 1 and II C 2. The planar interface yields for all considered thicknesses a higher reabsorption than the Lambertian interface [cf. Fig. 2(a)]. The reason for the larger reabsorption in the planar multilayer is the suppression of coupling to modes sustained in air due to total internal reflection and prevalent coupling to waveguide modes. On the other hand, the Lambertian texture provides many coupling channels, which leads to a large out-coupling and a lower portion of power that is absorbed. The slightly

oscillating behavior of the reabsorption for the planar interface stems from Fabry-Pérot resonances in the thin-film layer.¹⁵ These oscillations in the reabsorption spectrum are stronger for each individually simulated emitter position but can still be seen in the averaged reabsorption.

We used Eq. (1) to calculate from the reabsorption the open-circuit voltage enhancement ΔV_{oc}^{PR} . A similar trend like in the reabsorption can also be observed for ΔV_{oc}^{PR} [cf. Fig. 2(b)]: The higher reabsorption in the planar case directly translates to a higher achievable ΔV_{oc}^{PR} for the planar structure. A nanopatterned structure is expected to fall somewhere between these two cases, and it will be the goal of the further analysis to deduce the open-circuit voltage enhancement for a highly relevant grating geometry for solar cell devices, namely, a two-dimensional periodic grating.

From the various numerical simulations that concern the grating structures, we consider at first the angular spectra of the simplified stack that are depicted in Fig. 3. For the three plots, different grating periods and perovskite layer thicknesses have been used, whereas the grating depth was set to 110 nm throughout. Figure 3(a) was calculated for a period of 400 nm and a perovskite thickness of 200 nm. The parameters used in Fig. 3(b) were 400 nm period and 250 nm thickness of perovskite. Finally, for Fig. 3(c), the period was 450 nm and the perovskite thickness was 200 nm.

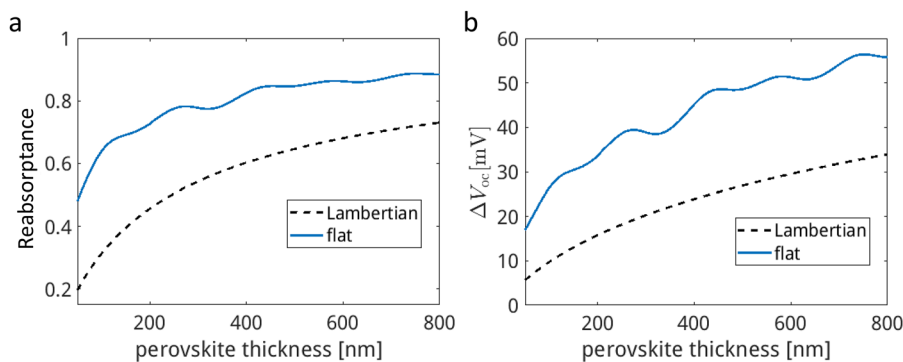


FIG. 2. (a) Reabsorption of radiatively emitted light in perovskite with a planar and Lambertian perovskite/air interface for different perovskite thicknesses resulting from a dipole emitter. The emission wavelength is 780 nm. (b) Corresponding achievable open-circuit voltage enhancement due to photon recycling, calculated with Eq. (1).

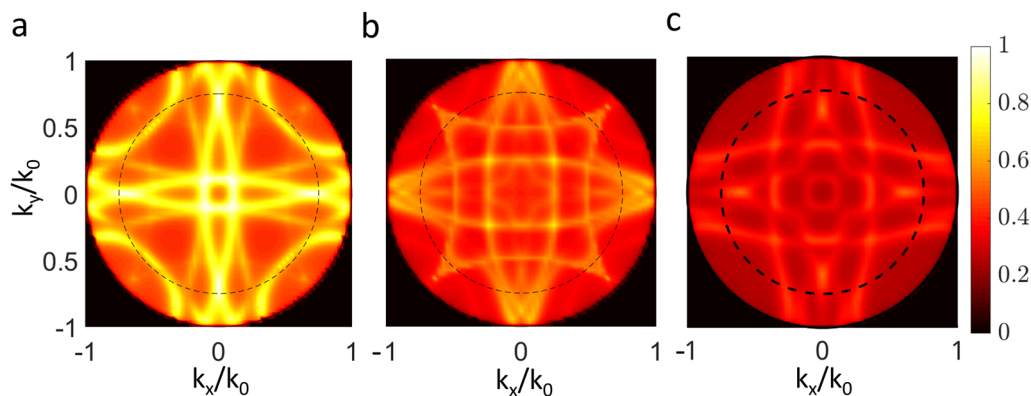


FIG. 3. Calculated angular spectra of the perovskite emission at a wavelength of 780 nm and for a hole depth of 110 nm. (a) Grating period 400 nm and perovskite thickness 200 nm. (b) Grating period 400 nm and perovskite thickness 250 nm. (c) Grating period 450 nm and perovskite thickness 200 nm. The dashed lines have a radius of 0.75 and mark the numerical aperture of the objective used in the measurement, while the radius of the visible angular spectrum corresponds to the air light line.

We generally observe that the outcoupled radiation shows strong angular dependency. For increasing thickness and increasing period, the most intense far field components shift to larger wave vectors. Due to the simultaneously increasing absorption and decreasing radiation, the total intensity of the far field decreases. This is apparent in Fig. 3, where for all three angular spectra the same normalization was used. Especially in Fig. 3(a), the spectrum also shows strong additional features near the light line, which indicates that light is scattered into air in quite large angles.

The visual appearance of the angular spectra can be explained by looking at the guided eigenmodes sustained in unstructured multilayer stacks. In Fig. 4(a), we show the available guided modes for different thicknesses of the perovskite layer. For example, at a thickness of 200 nm, three modes are available: the fundamental TE₀ and TM₀ modes and the TE₁ mode. However, the latter one is very weak and therefore negligible. Figures 4(b) and 4(c) show the intensity distributions of the two lowest order modes in the planar multilayer system. Strong dependency of the intensity distribution along the *z*-axis can be observed. For the TE₀ mode, the intensity peak is quite in the center of the perovskite layer, while for the TM₀ mode, a large portion of the intensity is leaking into the ITO layer, thereby leading to large parasitic absorption. This high spatial dependency of the modes demands for calculating the emission response at many different *z*-positions, as was done in our work.

In Fig. 4(d), these two modes for a perovskite thin film with a thickness of 200 nm have been folded into the first Brillouin zone, assuming a periodicity of 400 nm and a vacuum wavelength of 780 nm. The effective refractive indices inside the perovskite layer for the example thickness of 200 nm are $n_{TE_0} = 2.28$ as well as $n_{TM_0} = 2.04$.

Comparing Fig. 3 with Fig. 4(d), we can observe that coupling to the TE₀ and TM₀ modes is the most dominant contribution to the emission spectrum. In Fig. 3(a), we can identify four strong features at normalized in-plane wave vectors with an amplitude of approximately 0.15 each that stem from the intersection of the TE₀ and TM₀ dispersion lines. It seems that the propagation constants of the TM₀

and TE₀ modes are slightly changed in the presence of the grating so that their dispersion curves coincide with each other. For the TM₀ mode, this might be because it has a large intensity in the spatial region of the perovskite/air interface [see Fig. 4(c)], which leads to a power redistribution in the presence of the grating perturbation. As one can deduce from Fig. 4(a), a larger thickness of the perovskite leads to larger effective refractive indices of the modes, which in turn leads to the intensity peaks of the far field being located at larger *k*-values. This is exactly what we observe in our calculated angular spectra shown in Figs. 3(a) and 3(c). In Fig. 3(a), additional dispersion lines can be seen near the light line, which belong also to the fundamental TE₀ and TM₀ modes, but are shifted by an additional reciprocal grating vector. A larger grating period implies a smaller displacement of the dispersion circles in reciprocal space. This is consistent with Fig. 3(c), where the circular segments of two dispersion circles that are displaced by a positive and a negative reciprocal unit vector, respectively, are farther away from each other.

Despite that slight deviations, we can conclude that the grating, although it encompasses a large portion of the thickness of the perovskite layer, only acts as a small perturbation to the photonic eigenmodes of the multilayer stack, without fundamentally changing the available modes and their dispersion relations. The fact that the strongest emission features occur at distinct $k_{||}$ values could be envisioned to be exploited by an angular restriction of the escape cone, which might strongly decrease the radiated power and increase the absorbance in the perovskite layer.

In Fig. 5, we show results of measurements of the photoluminescent emitted power from selected samples. Depicted are the angular spectra that were collected as described in Sec. II B. The three figures show results for different periods between ~410 nm and ~460 nm. From scanning-electron microscope images (see the [supplementary material](#)), we can approximately deduce perovskite layer thicknesses between ~200 nm and ~310 nm for the different nanopatterned samples. From the SEM micrographs, we also obtain an average hole depth of around 110 nm. We can identify the same characteristic dispersion curves consisting of a

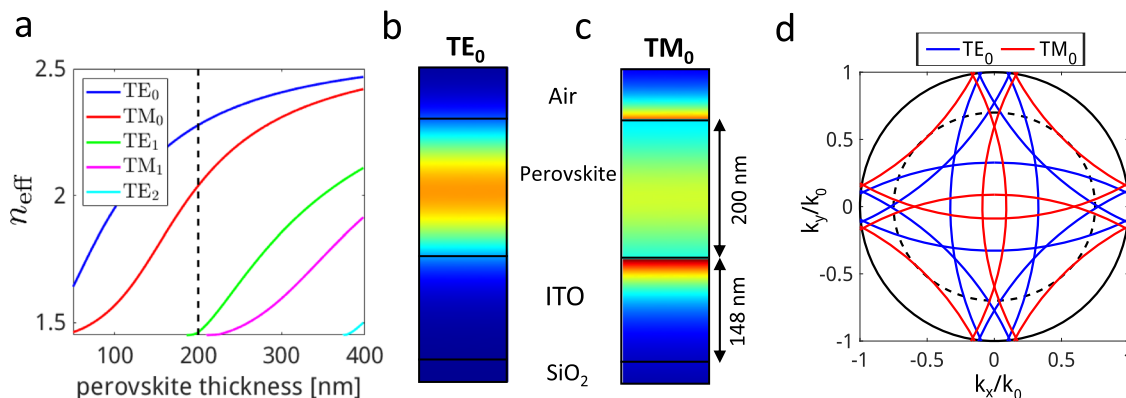


FIG. 4. (a) Effective refractive indices of the available modes in the planar multilayer system for increasing thickness of the perovskite layer. Spatially resolved intensity of the fundamental TE₀ (b) and TM₀ (c) modes present in the multilayer stack for a perovskite thickness of 200 nm. (d) Dispersion curves of the fundamental TE₀ and TM₀ modes assuming a period of 400 nm and a perovskite thickness of 200 nm. The dashed circle indicates the numerical aperture of 0.75 that was used in the measurements, and the solid circle is the light line in air.

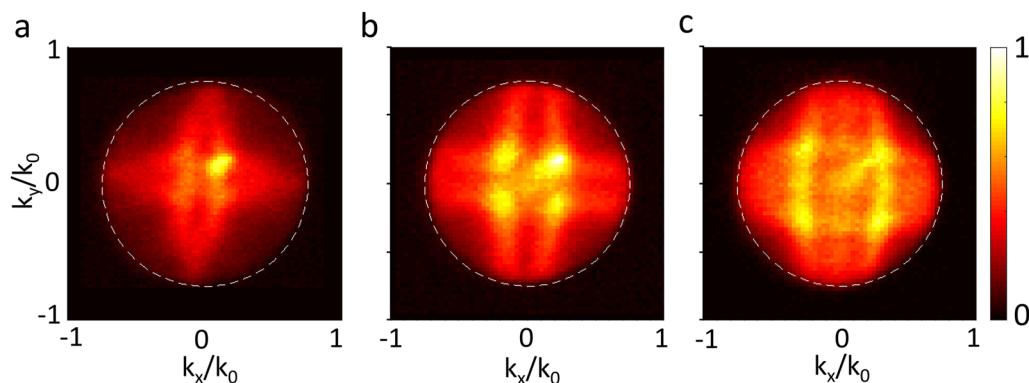


FIG. 5. Measured angular spectra of the perovskite emission using different grating periods. (a) Grating period ~ 410 nm, (b) grating period ~ 430 nm, and (c) grating period ~ 460 nm. In agreement with the numerical results in Figs. 3 and 4, the intensity peaks shift to larger k -vectors when the period is increased. The white dashed circle indicates the numerical aperture of 0.75 in the measurements.

double cross and symmetric intensity peaks at certain k_{\parallel} values that depend on the period. The minor features that are visible in the simulations cannot be identified in the measurements, which might be due to insufficient sensitivity of the detector. Furthermore, the perovskite thickness of the measured samples was not totally constant for an individual sample, which might introduce further deviations from the simulation results. Having in mind these possible sources for deviations, we can still assume that our numerical approach reproduces well the physics of the considered system.

We can thus proceed to calculate the enhancement of the open-circuit voltage in the presence of the grating due to photon recycling for both considered layer stacks. In the following, we will use Eq. (1) and assume that the internal quantum luminescence $Q_{\text{lum}} = 1$ and the device is operated under $T = 300$ K. As a reference, the open-circuit voltage enhancements for a 200 nm thick planar and a Lambertian texture, respectively, are $\Delta V_{\text{oc}}^{\text{PR}} = 33.5$ mV and $\Delta V_{\text{oc}}^{\text{PR}} = 15.8$ mV [cf. Fig. 2(b)]. The relatively large value for the planar texture is due to coupling to waveguide modes and total internal reflection, which both effectively suppresses the out-coupling into modes sustained in air. Conversely, the Lambertian provides many scattering channels into leaky waveguide modes, which strongly reduces the absorbance in the perovskite layer.

From our simulations of the simplified stack, we find that $\Delta V_{\text{oc}}^{\text{PR}}$ for the geometries with our nanostructure yields values between the corresponding Lambertian and flat textures. Among the simulated nanotextures, the one with a perovskite thickness of 250 nm and a period of 400 nm [Fig. 3(b)] shows the largest absorbance; it amounts to $p_{\text{abs}} = 0.61$, which in turn leads to $\Delta V_{\text{oc}}^{\text{PR}} = 24.3$ mV. We attribute this to the larger absorber volume compared to the other two considered textures. For the simulation of the nanotexture geometry with period 400 nm and thickness 200 nm [Fig. 3(a)], the absorbance is $p_{\text{abs}} = 0.51$ and the resulting $\Delta V_{\text{oc}}^{\text{PR}} = 18.4$ mV. Finally, the absorbance in the nanostructure with a period of 450 nm and a thickness of 200 nm [Fig. 3(c)] is $p_{\text{abs}} = 0.55$, yielding $\Delta V_{\text{oc}}^{\text{PR}} = 20.8$ mV, which is an $\sim 30\%$ increase compared to the aforementioned 15.8 mV for the Lambertian texture.

In the next step, we computed $\Delta V_{\text{oc}}^{\text{PR}}$ for the complete solar cell stack, as depicted in Fig. 1(c). Such nanotextured multilayer systems have been experimentally shown in several publications to yield an enhanced efficiency as compared to planar multilayers.^{23,40} We use the following layer thicknesses: ITO 148 nm, TiO_2 20 nm, and Spiro-OMeTAD 230 nm. The glass substrate and gold back reflector are modeled as semi-infinite half-spaces. Furthermore, we calculate $\Delta V_{\text{oc}}^{\text{PR}}$ for two different perovskite thicknesses, 200 nm and 250 nm, where the imprinted holes have the same geometric parameters as for the simplified layer. For the 200 nm thick perovskite layer, $\Delta V_{\text{oc}}^{\text{PR}} = 24.0$ mV, whereas for the 250 nm thick perovskite layer, $\Delta V_{\text{oc}}^{\text{PR}} = 28.3$ mV.

As one can expect, these values are higher than those for the simplified stack due to the presence of the gold back reflector, which decreases the amount of power that escapes the layer stack. However, the additional layers are accompanied with additional parasitic absorption, and therefore the increase in open-circuit voltage compared to the simplified multilayer is not dramatic. The fact that we assume optimal collection efficiency and the necessary introduction of nonabsorbing layers affect the results in the opposite way. The obtained values for $\Delta V_{\text{oc}}^{\text{PR}}$ can therefore serve as a good estimate of what can be expected in a nanostructured thin-film perovskite solar cell.

To obtain a full picture, we also calculated the short-circuit current density j_{sc} for the simplified stack. We compare the nanotextured structure with period 400 nm and perovskite thickness 200 nm to a planar multilayer with the same perovskite volume (i.e., the perovskite thickness was chosen to be 156 nm) to enable a fair comparison. For the planar multilayer, we get $j_{\text{sc}}^{\text{plan}} = 16.3 \frac{\text{mA}}{\text{cm}^2}$, while for the nanotextured structure, we obtain $j_{\text{sc}}^{\text{grat}} = 18.1 \frac{\text{mA}}{\text{cm}^2}$. This confirms that nanotexturing has a considerable effect on the short-circuit current density. Using the complete solar cell stack, a further increase of around 10% for the nanopatterned structure can be achieved.²⁴

These results highlight that to obtain maximal efficiency, the primary objective should be to optimize the light-incoupling into the absorber layer since this directly translates to an enhanced short-circuit current density. Additionally, considering photon recycling

might have an additional small effect on the total efficiency. This means that, when the light-trapping properties have been optimized and several equivalent structures in terms of efficiency have been found, then the optical design of the solar cells might be further improved by exploiting photon recycling effects. Since photon recycling is only relevant for large internal quantum efficiency,²⁰ i.e., for high-quality materials, it might play a noticeable role in future high-efficiency devices.

IV. SUMMARY

In this work, we investigated the impact of nanostructured perovskite regarding the achievable open-circuit voltage enhancement due to photon recycling. We simulated and measured the emission spectrum that occurs in perovskite layers due to electron-photon recombination. The position and orientation averaged emission far-field spectrum obtained from the calculations is in good agreement with the measurements and displays strong directionality that stems from coupling to leaky waveguide modes sustained by the multilayer. Our calculations also show that a major portion of reemitted photons is expected to be reabsorbed in the nanostructured perovskite layer. We find that our nanopattern shows a larger photon recycling rate than the ideal Lambertian case. While the optimization of nanostructures for light-trapping purposes still should be the primary goal, our analysis shows the necessity to also take into account the secondary effect of photon recycling for a holistic evaluation of solar cell performance.

SUPPLEMENTARY MATERIAL

See [supplementary material](#) for a schematic sketch illustrating the experimental setup of the back-focal plane measurements, the spectrally resolved photoluminescence peak of the perovskite used for the measurements, the detailed analytical derivation of the reabsorption in the perovskite layer in the presence of the Lambertian interface, and the SEM cross sections of the perovskite samples used for the measurements.

ACKNOWLEDGMENTS

We acknowledge support from the Deutsche Forschungsgemeinschaft (DFG) through Program DFG-SPP 1839 “Tailored Disorder” (RO 3640/6-2, Project-ID 278744673), the Excellence Cluster “3D Matter Made to Order” (3DMM2O) (EXC-2082, Project-ID: 390761711), and the Karlsruhe School of Optics and Photonics (KSOP). We also acknowledge the company JCMwave for kindly providing the software used for the simulations. We acknowledge support by Deutsche Forschungsgemeinschaft and Open Access Publishing Fund of Karlsruhe Institute of Technology. Furthermore, we thank Jonas Schwenzer for helping with the preparation of the samples. G.G. also acknowledges support from the Helmholtz Postdoc Program. U.W.P. acknowledges financial support of the Bundesministerium für Bildung und Forschung (PRINTPERO) and the Initiating and Networking funding of the Helmholtz Association [HYIG of Dr. U.W. Paetzold; the Helmholtz Energy Materials Foundry (HEMF); and PEROSEED].

REFERENCES

- F. Staub, H. Hempel, J.-C. Hebig, J. Mock, U. W. Paetzold, U. Rau, T. Unold, and T. Kirchartz, *Phys. Rev. Appl.* **6**, 044017 (2016).
- M. H. Futscher and B. Ehrler, *ACS Energy Lett.* **1**, 863 (2016).
- W. Tress, *Adv. Energy Mater.* **7**, 1602358 (2017).
- Z. Liu, L. Krückemeier, B. Krogmeier, B. Klingebiel, J. A. Marquez, S. Levchenko, S. Öz, S. Mathur, U. Rau, T. Unold, and T. Kirchartz, *ACS Energy Lett.* **4**, 110 (2019).
- M. A. Green, A. Ho-Baillie, and H. J. Snaith, *Nat. Photonics* **8**, 506 (2014).
- P. Brenner, M. Stulz, D. Kapp, T. Abzieher, U. W. Paetzold, A. Quintilla, I. A. Howard, H. Kalt, and U. Lemmer, *Appl. Phys. Lett.* **109**, 141106 (2016).
- P. Brenner, T. Glöckler, D. Rueda-Delgado, T. Abzieher, M. Jakoby, B. S. Richards, U. W. Paetzold, I. A. Howard, and U. Lemmer, *Opt. Mater. Express* **7**, 4082 (2017).
- J.-P. Correa-Baena, M. Saliba, T. Buonassisi, M. Grätzel, A. Abate, W. Tress, and A. Hagfeldt, *Science* **358**, 739 (2017).
- S. V. Makarov, V. Milichko, E. V. Ushakova, M. Omelyanovich, A. C. Pasaran, R. Haroldson, B. Balachandran, H. Wang, W. Hu, Y. S. Kivshar, and A. A. Zakhidov, *ACS Photonics* **4**, 728 (2017).
- X. Zhang, J.-X. Shen, W. Wang, and C. G. V. de Walle, *ACS Energy Lett.* **3**, 2329 (2018).
- J. E. Parrott, *Sol. Energy Mater. Sol. Cells* **30**, 221 (1993).
- V. Badescu and P. T. Landsberg, *Semicond. Sci. Technol.* **12**, 1491 (1997).
- L. M. Pazos-Outon, M. Szumilo, R. Lamboll, J. M. Richter, M. Crespo-Quesada, M. Abdi-Jalebi, H. J. Beeson, M. Vrucinic, M. Alsari, H. J. Snaith, B. Ehrler, R. H. Friend, and F. Deschler, *Science* **351**, 1430 (2016).
- Z. Gan, W. Chen, L. Yuan, G. Cao, C. Zhou, S. Huang, X. Wen, and B. Jia, *Appl. Phys. Lett.* **114**, 011906 (2019).
- T. Kirchartz, F. Staub, and U. Rau, *ACS Energy Lett.* **1**, 731 (2016).
- T. Yamada, Y. Yamada, Y. Nakaïke, A. Wakamiya, and Y. Kanemitsu, *Phys. Rev. Appl.* **7**, 014001 (2017).
- W. E. I. Sha, X. Ren, L. Chen, and W. C. H. Choy, *Appl. Phys. Lett.* **106**, 221104 (2015).
- J. M. Richter, M. Abdi-Jalebi, A. Sadhanala, M. Tabachnyk, J. P. Rivett, L. M. Pazos-Outon, K. C. Gödel, M. Price, F. Deschler, and R. H. Friend, *Nat. Commun.* **7**, 13941 (2016).
- T. Tayagaki, K. Makita, R. Oshima, H. Mizuno, and T. Sugaya, *Opt. Express* **27**, A1 (2019).
- M. G. Abebe, A. Abass, G. Gomard, L. Zschiedrich, U. Lemmer, B. S. Richards, C. Rockstuhl, and U. W. Paetzold, *Phys. Rev. B* **98**, 075141 (2018).
- C. H. Swartz, S. Paul, L. M. Mansfield, and M. W. Holtz, *J. Appl. Phys.* **125**, 053103 (2019).
- T. K. Nguyen, P. T. Dang, and K. Q. Le, *J. Opt.* **18**, 125901 (2016).
- Y. Wang, P. Wang, X. Zhou, C. Li, H. Li, X. Hu, F. Li, X. Liu, M. Li, and Y. Song, *Adv. Energy Mater.* **8**, 1702960 (2018).
- R. Schmager, G. Gomard, B. S. Richards, and U. W. Paetzold, *Sol. Energy Mater. Sol. Cells* **192**, 65 (2019).
- H. Wang, S.-C. Liu, B. Balachandran, J. Moon, R. Haroldson, Z. Li, A. Ishteev, Q. Gu, W. Zhou, A. Zakhidov, and W. Hu, *Opt. Express* **25**, A1162 (2017).
- I. M. Hossain, D. Hudry, F. Mathies, T. Abzieher, S. Moghadamzadeh, D. Rueda-Delgado, F. Schackmar, M. Bruns, R. Andriessen, T. Aernout, F. D. Giacomo, U. Lemmer, B. S. Richards, U. W. Paetzold, and A. Hadipour, *ACS Appl. Energy Mater.* **2**, 47 (2019).
- M. van Eerden, M. Jaysankar, A. Hadipour, T. Merckx, J. J. Schermer, T. Aernouts, J. Poortmans, and U. W. Paetzold, *Adv. Opt. Mater.* **5**, 1700151 (2017).
- N. Pourdavoud, S. Wang, A. Mayer, T. Hu, Y. Chen, A. Marianovich, W. Kowalsky, R. Heiderhoff, H.-C. Scheer, and T. Riedl, *Adv. Mater.* **29**, 1605003 (2017).
- H. Wang, R. Haroldson, B. Balachandran, A. Zakhidov, S. Sohal, J. Y. Chan, A. Zakhidov, and W. Hu, *ACS Nano* **10**, 10921 (2016).
- A. Mayer, M. Buchmüller, S. Wang, C. Steinberg, M. Papenheim, H.-C. Scheer, N. Pourdavoud, T. Haeger, and T. Riedl, *J. Vac. Sci. Technol., B: Microelectron. Process. Phenom.* **35**, 06G803 (2017).

- ³¹J. Pomplun, S. Burger, L. Zschiedrich, and F. Schmidt, *Phys. Status Solidi B* **244**, 3419 (2007).
- ³²J.-P. Berenger, *J. Comput. Phys.* **114**, 185 (1994).
- ³³S. M. Barnett, B. Huttner, R. Loudon, and R. Matloob, *J. Phys. B: At., Mol. Opt. Phys.* **29**, 3763 (1996).
- ³⁴C. T. Tai and R. E. Collin, *IEEE Trans. Antennas Propag.* **48**, 1501 (2000).
- ³⁵M. A. Green, *Prog. Photovoltaics* **10**, 235 (2002).
- ³⁶L. Zschiedrich, H. J. Greiner, S. Burger, and F. Schmidt, *Proc. SPIE* **8641**, 86410B (2013).
- ³⁷U. Rau, U. W. Paetzold, and T. Kirchartz, *Phys. Rev. B* **90**, 035211 (2014).
- ³⁸S. Jain, V. Depauw, V. D. Miljkovic, A. Dmitriev, C. Trompoukis, I. Gordon, P. V. Dorpe, and O. E. Daif, *Prog. Photovoltaics* **23**, 1144 (2015).
- ³⁹ASTM, Standard Tables for Reference Solar Spectral Irradiances: Direct Normal and Hemispherical on 37° Tilted Surface, American Society for Testing and Materials, West Conshohocken, PA, 2012, available from <https://www.astm.org>.
- ⁴⁰W. Kim, M. S. Jung, S. Lee, Y. J. Choi, J. K. Kim, S. U. Chai, W. Kim, D.-G. Choi, J. H. C. H. Ahn, D. Choi, H. Shin, D. Kim, and J. H. Park, *Adv. Energy Mater.* **8**, 1702369 (2018).